HiSST: 4th International Conference on
High-Speed Vehicle Science & Technology
22–26 September 2025, Tours, France

Flight Stability Analysis and Flap Size Optimization along a Trajectory of a Waverider Concept

Marius Franze[1], *Fynn Barz*[2]

Abstract

The High Lift Reentry Vehicle (HLRV) and its reference trajectory introduced in earlier studies will serve as the baseline for the work in this paper. The generic waverider is utilized for code-to-code validation and comparison due to its simple geometry features and short solution times. First, results of an implemented low-fidelity Second Order Shock Expansion as well as Modified-Newton codes gets compared to simulated data of the high-fidelity DLR TAU code. Especially in combination on specific geometric features, e.g. computation of blunt leading edges using the Modified-Newton mehtod and SOSE otherwise, the results show great agreement in the quantitative as well as excellent agreement in the overall trend of the analyzed body fixed forces and pitching moments along the trajectory. The validated panel codes are then employed to map the HLRV's static pitching-stability envelope over the entire trajectory, revealing that a waverider with a center of gravity of 60 % of its length remains stable in its trimmed configuration, whereas the uniformly mass-distributed vehicle becomes unstable without flap deployment. Free-flight simulations in the trimmed state demonstrate that the baseline HLRV can be trimmed with flap deflections under 4° at trim angles between 2° to −3°. Leveraging the DLR SMARTy optimization toolbox, surrogate models are generated along the trajectory to optimize the upper and lower flap sizes while preserving pitch stability. Two separate optimizations are performed: (I) minimizing drag and (II) maximizing lift-over-drag ratio, establishing the performance bounds of the reference HLRV. Several optimal geometries have been identified on the resulting Pareto front, depending on the objective functions. The integrated multi-point optimization chain accelerates aerodynamic and aerothermal load predictions, enabling low-fidelity tools to be used for targeted analyses such as pitch-stability assessment. This facilitates broader optimization strategies, improves thermal-protection-system design, and supports the development of more efficient hypersonic reentry vehicles.

Keywords: High Lift Reentry Vehicle, Waverider, Multi-Fidelity, Surrogate, Optimization, Flight-Stability Analysis

Nomenclature

Abbreviations

CFD	Computational Fluid Dynamics
CoNF^{2}aS^2	Coupled Numerical Fluid Flight Mechanic and Structure Simulation
DOE	Design of Experiment
EI	Expected Improvement
FSI	Fluid-Structure-Interaction
HLRV	High Lift Reentry Vehicle
LHS	Latin Hypercube Sampling
LoD	Lift over Drag
MN	Modified-Newton
MP	Matching-Point
SBO	Surrogate Based Optimization
SE	Shock Expansion
SMARTy	Surrogate Modeling for Aero-Data Toolbox in python
TR	Trust Region
WR	Waverider

[1] *German Aerospace Center (DLR), Institute of Aerodynamics and Flow Technology, Spacecraft, Lilienthalplatz 7, 38108 Braunschweig, Germany, Marius.Franze@dlr.de*

[2] *German Aerospace Center (DLR), Institute of Aerodynamics and Flow Technology, Spacecraft, Lilienthalplatz 7, 38108 Braunschweig, Germany, Fynn.Barz@dlr.de*

Subscripts

D	Drag
lee	Leeside of the Vehicle
max	Maximal Value
min	Minimal Value
ref	Reference Values
wind	Windwardside of the Vehicle

Greek

α	Angle of Attack
ϵ	Relative Error
η	Flap deflection Angle

Latin

C	Dimensionless Coefficient
h	Altitude
M	Mach Number
p	Pressure
r_{LE}	Leading Edge Radius
T	Temperature
t	Time of Flight
u	Velocity
x, y, z	Coordinates

1. Introduction

The generic High Lift Reentry Vehicle (HLRV) and its reference trajectory, introduced in [24] and [6] will serve as the baseline for the work in this paper. The waverider (WR) geometry is utilized for code-to-code validation and comparison due to its simple geometry features, thereby establishing a foundation for a multi-fidelity computational approach, which will be employed within the optimization toolbox DLR SMARTy [7]. This enables the use of machine learning (ML) trained with high-fidelity computational fluid dynamics (CFD) data as presented in [30] and further improves it with its multi-fidelity capabilities. In the future, a multi-fidelity workflow will be implemented and used to accelerate the design process while maintaining the accuracy of the high-fidelity methods by using machine learning (ML) and artificial intelligence (AI) methods to select the specific methods along a trajectory. The goal is to use the faster methods along a broad design space and afterwards re-evaluating the error and reducing it with the more accurate but computationally expensive methods.

This present study focuses on the pitching maneuverability, which is one of the most critical performance criteria for an HLRV during reentry. The spacecraft needs to catch itself quickly enough with the maximum available lift before encountering dense atmospheric regions, which would otherwise result in high aerothermal loads.

From the perspective of unsteady numerical analysis, high-lift reentry vehicles experience long glide phases, making high-resolution simulations computationally demanding, with cost strongly dependent on the level of the fidelity of the simulated physics of the flow. Conversely, wind-tunnel experiments are limited by achievable test duration, measurement accuracy, or both, particularly at high Mach numbers where real-gas effects become significant. Full-scale reentry flight tests are likewise costly, especially when aiming to reproduce authentic flight conditions with geometrically accurate prototypes.

To analyze the complex flow phenomena and associated heating mechanisms encountered by high-lift reentry vehicles in hypersonic conditions, a high-fidelity, fully coupled fluid/structure/flight-mechanics simulation environment was employed. The flow field and resulting internal heat loads were computed for a representative vehicle following a generic reentry trajectory [24], displayed in figure 1. Coupling between the individual solvers was realized through the FlowSimulator framework, which incorporates the CoNF^{2}aS^2 (Coupled Numerical Fluid-Flight-mechanics and Structure Simulation) environment. The FlowSimulator provides efficient parallel data management, interpolation, and exchange among heterogeneous solvers and has been advanced toward the objective of virtual flight testing [41, 38]. Its modular architecture permits the integration of CoNF^{2}aS^2 as a core component, onto which spacecraft-specific models can be appended, thereby delivering a flexible and versatile tool chain.

For the high fidelity reference purpose, fully unsteady three-dimensional fluid calculations have been performed applying an equilibrium and non-equilibrium gas model on the computational fluid side [24]. It is time accurately strongly coupled with a higher order structural solver using temperature dependent non-linear material models for the computed bodies. The fluid as well as structural solver uses methods

of second order in space and time. These models and coupling procedures are very time consuming and computationally intensive. Even on a high performance cluster system, these coupled simulations can easily take months to analyze a complete trajectory.

To speed up the coupled environment to the point of optimization capabilities during the design process, lower fidelity models for fluid solving are integrated in CoNF^{2}aS^2 and first results are presented in this paper. These models are much faster, but lack the accuracy of the high fidelity models. The comparison of these models along each other by means of the generic HLRV is the first goal and main result of this paper to get an overall idea of the error range for the used lower fidelity methods as presented in chapter 4.1.

Detailed analysis using fluid-structure interaction (FSI) simulation on particular vehicle features, like ramps [43], control surfaces [35], inlets [48, 28] or simplified 2D geometries [40] have been performed at certain flight points. These lack the unsteady characteristics of steep hypersonic reentry paths, which are under investigation in this work.

On the other side, some very fast conceptual design methods for trajectory optimization itself or shape optimization along hypersonic trajectories have been presented, which is mostly achieved using reduced order models (ROM) on the fluid side, often ignoring the structural response of the vehicle entirely [11, 10, 26, 19].

Time dependent corrections methods have been studied [52] for the thermal response of the structure, which covers a whole trajectory. These are unable to compute unsteady time accurate motions like pitching maneuvers, which are under investigation in this paper. Unsteady evaluations often cover panel aerothermoelastic behavior [25, 49] or concentrate the computational effort on certain physical effects, like ablation [36, 14].

Several coupling methods have been presented, covering FSI simulations at certain representative flight points, again replacing the fluid solver with ROM methods like *piston theory* [50], frequency domain solver [43] or radial basis function interpolating kriging surfaces [13, 12]. They conclude that these methods are only reasonable for steady aerodynamics and if the grid is tailored specifically for the flight condition. The fast methods used in this paper will be validated against the high fidelity DLR TAU solver, which will show reasonable differences from a fast design perspective.

Recent advances have focused on the application of neural-network-based machine-learning (ML) models that are trained on high-fidelity computational fluid-dynamics (CFD) datasets [30]. Although such models can achieve high predictive accuracy, their computational cost may become substantial, particularly when deep architectures with many layers and neurons are employed. In parallel, physics-informed ML surrogates for hypersonic trajectory optimization have been introduced, offering significantly reduced evaluation times relative to full-order CFD simulations while preserving essential physical fidelity [8].

The extensive fluid–structure-coupled post-flight analyses performed for hypersonic experimental programs such as BOLT [54, 15] and SHEFEX I [3] and II [23] has to be mentioned. Because the thermal interaction between the flow field and the vehicle structure is inherently unsteady, these experiments, together with dedicated fluid-structure-interaction (FSI) process chains, serve to validate the current generation of hypersonic fluid solvers and complete process chains.

As outlined above, hypersonic trajectory assessments span a spectrum from high- to low-fidelity methodologies. The objective is to create an auxiliary tool that can be incorporated into future multi-fidelity workflows for the aerothermal assessment of spacecraft vehicles. This gap will be filled by CoNF^{2}aS^2, which enables to analyze the flight path using low fidelity methods if possible and high fidelity models if necessary to reduce the computational effort as much as possible, while keeping the accuracy of the results.

2. Generic Use Case

2.1. Analyzed Trajectory

For reference purposes, a generic trajectory together with a representative vehicle geometry is used. Neither the trajectory nor the geometry corresponds to a specific real-world vehicle. They serve solely as benchmark cases to demonstrate the methodology. Consequently, they are intended as exemplary applications that conform to the physical and numerical limits of the solvers used in this study.

Figure 1 presents altitude h, angle of attack α and the corresponding mach number M over time of the generic trajectory. The motor separation at $t = 0\,\mathrm{s}$ is at an altitude of 85 km with a mach number of 12.3. This maneuver is followed by a dipping reentry curve down to 24.4 km at $t = 132\,\mathrm{s}$, pitching up to 32.3 km. Around 30 km the cruise phase starts at $t = 200\,\mathrm{s}$ with a mach number between 10.5 to 10.0. The angle of attack is varying between $\alpha = 12°$ during reentry and $-2°$ at the dipping point at the pitch up maneuver. During the glide phase it oscillates between 0° and 1° steadily converging towards 0°. The starting altitude of 85 km is selected to be at the boarder of validity of continuum flows with a mean free path of 0.01 m, as presented in [24]. For possible long range missions, a reference gliding altitude of 30 km was adopted from [17].

The points marked in the altitude plot are used for the surrogate model evaluation, described in chapter 4.3. They have an equal spacing of $\Delta t = 20\,\mathrm{s}$.

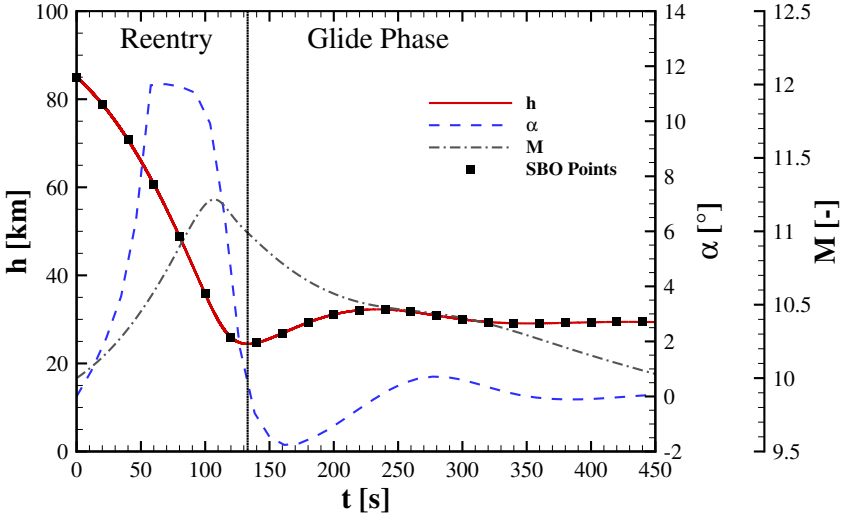

Fig 1. Generic trajectory including altitude, angle of attack and mach number for starting altitude at 85 km with marked points for surrogate evaluation.

2.2. Geometry of High Lift Reentry Vehicle

High-Lift Reentry Vehicles (HLRVs) typically exhibit lift-to-drag (LoD) ratios that far exceed those of conventional sounding rockets or reentry capsules. When viscous effects are incorporated during the design phase, LoD values in the range of 4–7 can be attained [17]. The HLRV shown in figure 2 achieves comparable ratios, depending on the selected trajectory and associated flight velocity.

The reference length of the vehicle is $l_{ref} = 3000\,\mathrm{mm}$ (excluding the rounded leading edge). The leading-edge radius is defined as $r_{LE} = 0.0015 \cdot L_{ref} = 4.5\,\mathrm{mm}$ which yields a tangential transition from the windward side to the lee side. Consequently, the effective overall length and maximum width are reduced to 2923 mm and 1144 mm, respectively. The chosen leading-edge ratio of 0.0015 follows the recommendation of Eggers [17], which represents a compromise between manufacturability and wave-drag minimisation. Body flaps are omitted from the high-fidelity simulations to reduce computational cost for the comparison, while low-fidelity simulations incorporate the body flaps during the optimization process of themselves.

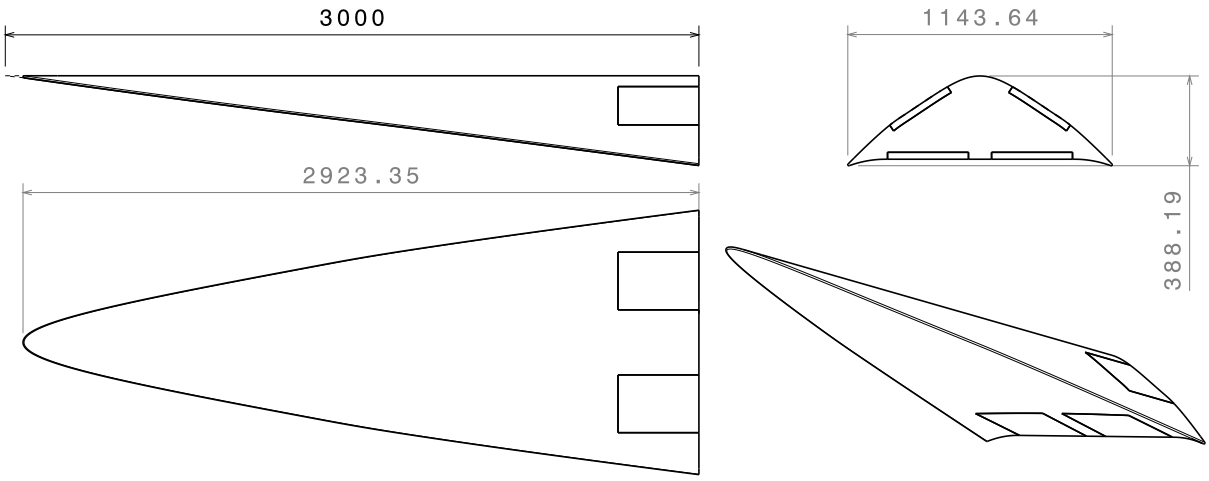

Fig 2. HLRV Geometry in different views and reference sizes in mm [24]

To assess the influence of the leading-edge geometry, two variants of the model are examined: one with a rounded leading edge and a second with a sharp leading edge, both illustrated in figure 2. The vehicle's main body shape was generated using the osculating-cone method at a number of 10. The semi-vertical angle between the vehicle's rotational axis and the conical shock is 10°, as described in detail by Barz [6].

3. Numerical Setup

Independent of the flow solver, the ICAO [39] atmosphere is used as atmospheric conditions and set at each calculated time step according to the flown altitude along the reference trajectory.

3.1. High Fidelity Approach - DLR TAU

For comparison and validation of the low fidelity solver simulations, the presented results from Franze [24], which are shown exemplary in figure 3 are reused in this paper. It utilized the DLR TAU code within a strong coupled FSI procedure of the partitioned single domain solver within CoNF^{2}aS^2.

DLR TAU is a three-dimensional, parallel, hybrid multigrid solver that has been validated for subsonic, transonic and hypersonic regimes (e.g., Schwamborn et al. [45], Langer et al. [32], Mack et al. [34]). The code integrates the Reynolds-averaged Navier-Stokes (RANS) equations with a second-order finite-volume discretisation and is optimised for large-scale simulations on high-performance-computing (HPC) clusters. Owing to its demonstrated efficiency, DLR TAU is employed extensively in both industrial and academic studies of steady and unsteady aerodynamics for complete air- and spacecraft configurations.

Among the available turbulence closures, the negative-formulation of the Spalart-Allmaras one-equation model [46] is adopted. This model has shown robust performance and adequate accuracy for high-speed vehicles [44].

For spatial discretisation of the convective fluxes, an AUSMDV flux-vector-splitting upwind scheme [51] is used, which remains applicable throughout the entire flight trajectory. To avoid uncertainties associated with laminar-to-turbulent transition, the vehicle walls are modelled as fully turbulent.

Figure 3(a) depicts the hybrid computational mesh employed for the fluid domain. The volumetric mesh comprises approximately 29.9 M nodes and 71.2 M elements, while the surface mesh contains about 0.72 M points. For a geometry of this complexity the mesh is comparatively fine resolved, a requirement for obtaining a smooth temperature distribution on the vehicle surface. Structured quadrilateral elements are used to discretise the rounded leading edge, whereas the remaining windward and leeward surfaces, together with the vehicle's base plane, are meshed with unstructured triangular elements to reduce the overall point count. A mesh-convergence analysis indicated a maximum discretisation error below 0.7 % (see [24] for further details).

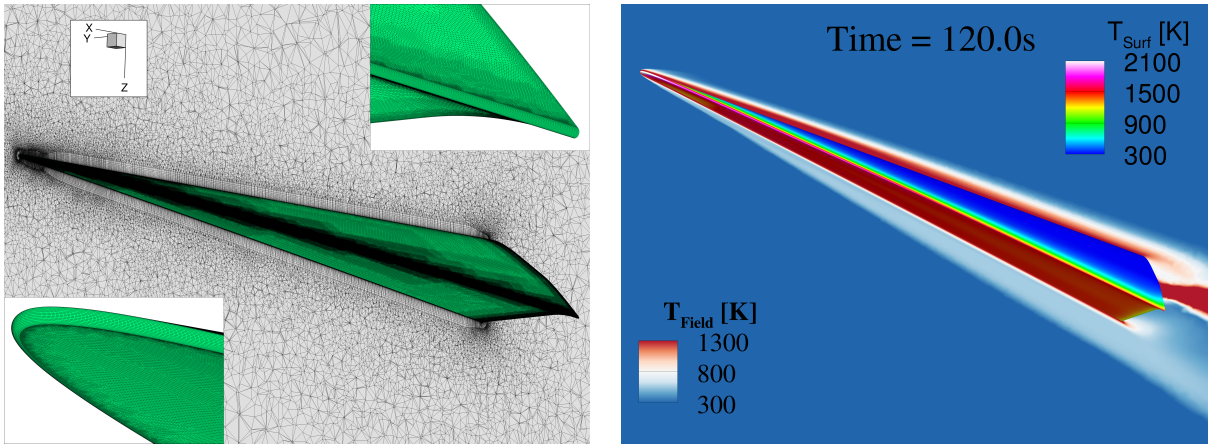

(a) CFD surface mesh and $y = 0$ slice.

(b) Selected flight point at $t = 120\,\mathrm{s}$.

Fig 3. CFD Mesh and selected flight point at $t = 120\,\mathrm{s}$ for illustration of the flow regime from [24].

Figure 3(b) gives a general impression of the occurring flow phenomena and high temperature gradients. The simulation has been accomplished using a five species chemical non equilibrium gas, (modelling N_2, O_2, NO, N, O), as described in the reference [24]. As these additions are only available in the spacecrafts version of DLR TAU, the results are label with *TauRF*.

3.2. Low Fidelity Approach - FSPanelCFD

Within the study, two variants of the WR geometry are analyzed. First, the geometry with a sharp leading edge and second, the WR with a blunt leading edge. Due to the difference in modelling the compression shock on the leading edges, different aerodynamic models need to be conducted.

For a sharp leading edge the shock remains attached when the flow is assumed inviscid. In this case the *Shock-Expansion* (*SE*) method [2] is employed. This technique is a local panel method: the flow properties and geometric characteristics of each panel are taken into account only. Starting at the leading-edge panel, the flow state is propagated downstream in an iterative fashion. The initial condition at the leading edge is obtained from the oblique-shock relations applied to the free-stream conditions. For each subsequent panel the appropriate relation is used: backward-facing (expansion) panels are treated with the Prandtl-Meyer expansion, whereas forward-facing (compression) panels are treated with the oblique-shock relations.

For a blunt leading edge a detached bow shock forms. The *Matching-Point* (*MP*) method [31], which combines the *Modified Newton* (*MN*) approach [2] with the shock-expansion method, is applied. The matching point is defined as the downstream location where the pressure and pressure gradient predicted by both methods become identical. Upstream of this point the flow behind the detached shock is determined with the *MN* method. Once the matching point is reached, the downstream flow is continued using the shock-expansion method described above.

It is known, that the shock expansion method suits slender sharp leading edged geometries and the *MN* method in contrast suits blunt bodies. For this reason the current implementation allows to set them on each boundary marker individually. The engineering approach, were the rounded leading is set to be calculated with the *MN* method and the wind and leewards sides of the HLRV are set to the *SE* method is labelled as *combined* method in the following results section in chapter 4.1.

The aerothermodynamic heating in the leading edge region can be calculated by combining the Fay-Riddell [20] equation with the cylinder correlation, as described in [53]. The Eckert reference temperature method [16] and solutions of the laminar or turbulent boundary layer equation [2, 9] are conducted in the region downstream of the matching point for the calculation of the heat flux and friction coefficients. Overall the implementations for the so called *FSPanelCFD* solver are described by Barz [6, 4].

4. Results

4.1. Numerical validation of low fidelity solver

To start the comparison between the low-fi solvers against high-fi results from DLR TAU (see reference [24]), the two methods *SE* and *MN*, which got described in the former chapter 3.2, are selected to individually predict the pressure distribution and forces and moment on the whole surface of the HLRV. Figure 4 presents the resulting body-fixed forces F_x and F_z as well as the pitching moment M_y.

In general, a qualitatively good trend can be seen in the results. On the other hand, quantitatively the differences are huge. Just comparing the values for DLR TAU and *SE* of the peak values at $t = 115.5\,\mathrm{s}$, which are located in the dipping phase of the trajectory, the relative differences are $\epsilon F_x = -21.1\,\%$, $\epsilon F_y = 10.6\,\%$ and $\epsilon M_z = 25.7\,\%$, as listed in table 1. Adding the friction prediction, presented with the added label *fric*, reduces the error only by a small amount to $\epsilon F_x = -12.8\,\%$, $\epsilon F_y = 10.5\,\%$ and $\epsilon M_z = 25.1\,\%$.

Even worse agreements can be notes for the pure *MN* approach. The differences gain to $\epsilon F_x = -41.6\,\%$, $\epsilon F_y = -31.1\,\%$ and $\epsilon M_z = -32.3\,\%$ in for the non-friction related values and improve just a little by adding the simple friction estimation.

As described earlier the *SE* method should only be applied to sharp geometries, which makes it hard to

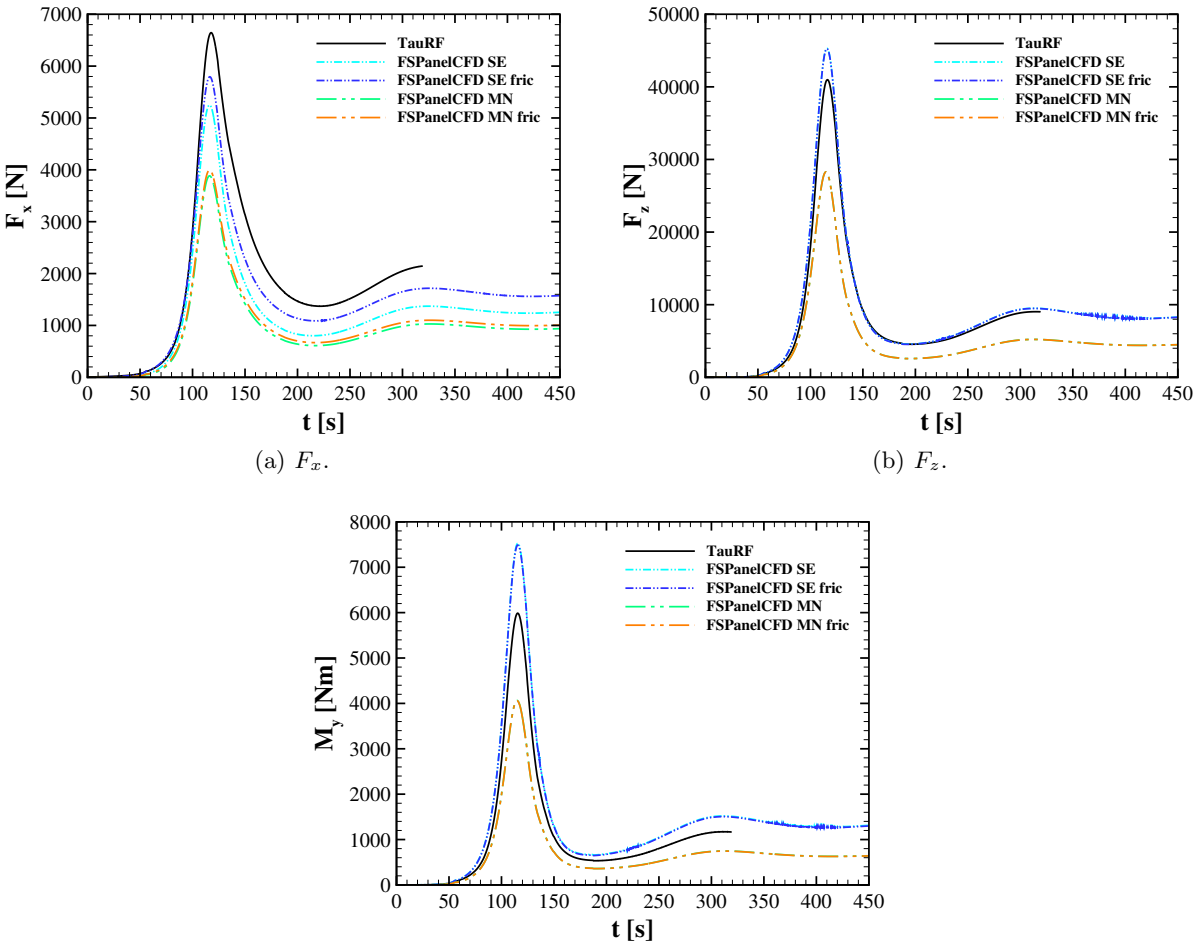

(a) F_x.

(b) F_z.

(c) M_y.

Fig 4. Comparison of F_x, F_z and M_y for Shock Expansion (*SE*) and Modified Newton (*MN*) against high-fidelity DLR TAU results from [24].

Table 1. Comparison of body-fixed Forces F_x, F_z and pitching moment M_y between low-fidelity solver FSPanelCFD and high-fidelity code DLR TAU.

Solver	Method	F_x [N]	$\epsilon(F_x)$ [%]	F_z [N]	$\epsilon(F_z)$ [%]	M_y [N m]	$\epsilon(M_y)$ [%]
DLR TAU	NEQ	6635.8		40944.6		5984.8	
FSPanelCFD	SE	5237.1	-21.1	45301.9	10.6	7525.1	25.7
	SE fric	5787.7	-12.8	45247.8	10.5	7487.2	25.1
	MN	3875.6	-41.6	28191.3	-31.1	4050.7	-32.3
	MN fric	3990.4	-39.9	28181.7	-31.2	4045.4	-32.4
	Comb	5335.9	-19.6	43690.9	6.7	6173.2	3.1
	Comb fric	5906.4	-11.0	43634.3	6.6	6134.5	2.5
	MP	362.4	-94.5	311.0	-99.2	262.8	-95.6
	MP fric	425.0	-93.6	305.1	-99.3	261.5	-95.6

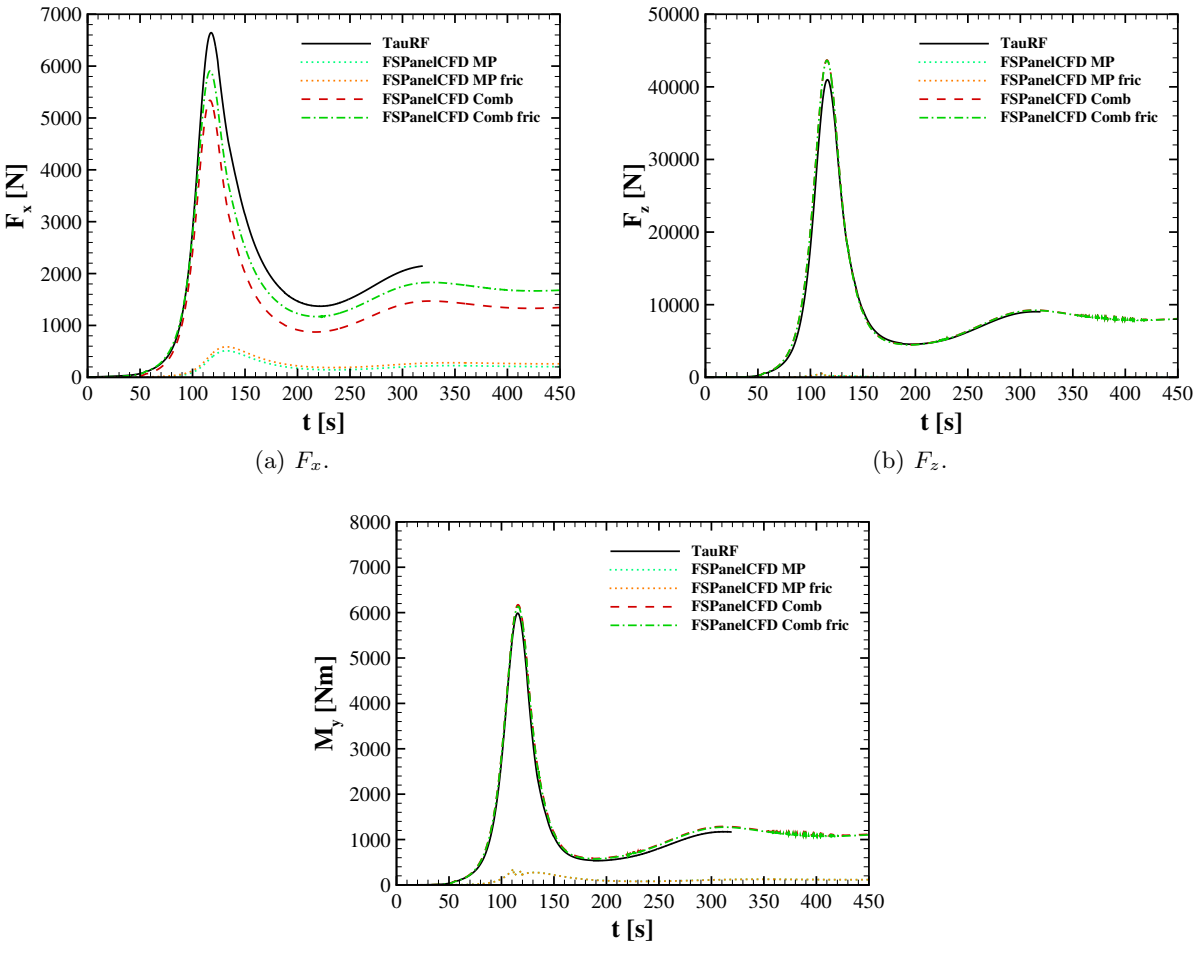

(a) F_x.

(b) F_z.

(c) M_y.

Fig 5. Comparison of F_x, F_z and M_y for Matching Point (*MP*) and Combined Method (*Comb*) against high-fidelity DLR TAU results from [24].

compare for presented the geometry with the rounded leading edges. Although the ratio leading edge to surface is only small (because $r_{LE} = 0.0015 \cdot L_{ref}$) the compared geometries are not identical, especially in its length, which will result in different leverage lengths. On the other side, the *MN* method only works well for blunt bodies. The results of the matching point (*MP*) method, which selects the transition point from one model to the other, are presented in figure 5. Unfortunately, the differences increase significantly. The simulation overpredicts the expansion at the rounded leading edge, followed by very small velocities on the streamwise downward panels, resulting in very low integral values overall.

As an engineering combined approach (*Comb*), the appropriate model get selected a priori, meaning *MN* at the blunt rounded leading edge and *SE* otherwise on the wind- and leeward surfaces as well as the flaps.

The comparison now shows very small differences in body forces (F_x, F_z) and pitching moment (M_y). Specifically, the peak pitching moment M_y differs by less than 3.1 % while F_z differs by less than 6.7 % and F_x less than 19.6 % for the frictionless case. Adding friction reduces the error down to $\epsilon F_x = -11.0\,\%$, $\epsilon F_y = 6.6\,\%$ and $\epsilon M_z = 2.5\,\%$. These results confirm that the panel code combinations are suitable for the following flap size optimization. Usually from an multi-fidelity optimization standpoint, it is sufficient for the low-fidelity solver to generate the overall trend of the values, which can be accomplished as the figures 4 and 5 present. Additionally, the panel codes generate very small differences to the high-fidelity CFD results for this reference geometry and trajectory.

For this reasons the *Comb* method is selected to providing simulation results for the following chapter to minimize drag (chapter 5.1) as well as increase lift over drag (chapter 5.2) providing improved gliding performance, while maintaining pitch stability.

4.2. Simple Trim Optimization

Next, the combination of panel codes, *MN* for the leading edges and *SE* for every other surface, are used to identify the pitching stability region of the HLRV along the entire trajectory from 1. It can be seen in figure 6(a) that the Waverider exhibits a broad band of statically stable region with a center of gravity smaller than 60 % of its length, which is typical for this type of vehicles. In contrast, an evenly distributed mass along the inner body results in a statically unstable vehicle, if the flaps are not deployed, with a center of gravity at around 67 % of the vehicle length.

To analyze the necessary flap deflection angles, free flight simulations demonstrate that the baseline Waverider can be pitch trimmed with flap deflections of under 4° at trim angles between 2° and −3° along the trajectory, as depicted in figure 6(b)

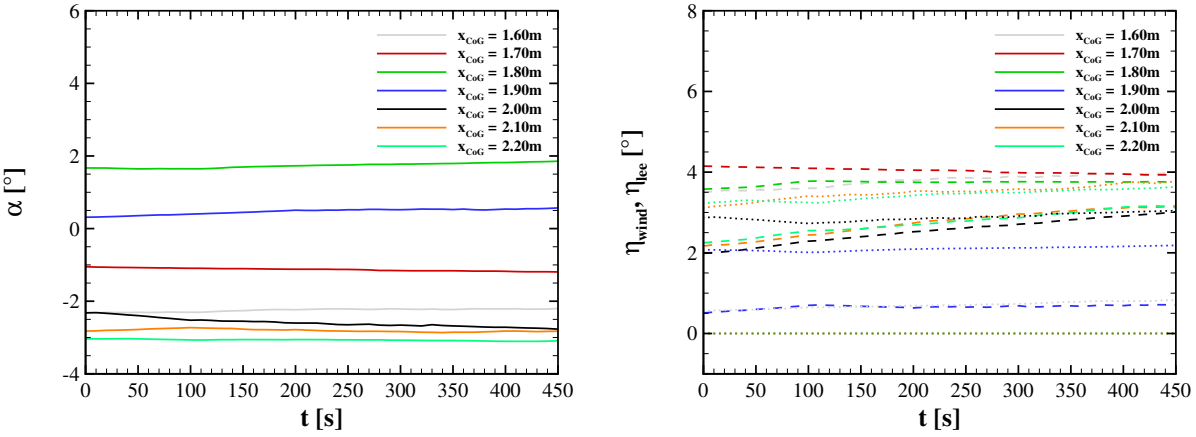

(a) x_{CoG}. (b) n_{luv}, n_{lee}.

Fig 6. Comparison of center of gravity and flap deflection angles in trimmed condition ($C_{my} = 0$).

The trim angle got identified using a simple *Nelder Mead Simplex* optimizer, which results only in the next local minima.

Finally, to improve flight performance for the geometry, the optimization framework DLR SMARTy is employed, as presented in [7]. Surrogate models are generated along the whole trajectory to optimize the upper and lower flap sizes, while maintaining its pitching stability. This enables the use of a variety of optimization techniques and models. In contrast to the very simple *Nelder Mead Simplex* method, SMARTy is capable of optimizing a much broader room and number of variables because of its implemented more sophisticated models and methods as described in the following chapter 4.3.

4.3. SMARTy - Surrogate Modelling Framework

The Surrogate Modelling Framework SMARTy (Surrogate Modeling for Aero-Data Toolbox in python) is an ongoing development by the DLR. Although a variety of models and methods are implemented the following subset of functionality is used in this paper.

The global optimizer adopts a modified surrogate-based optimization (SBO) strategy [29] that explicitly balances exploration against exploitation. At each iteration, an uncertainty quantification scheme based on the surrogate model is employed with an active infill to efficiently extract a specified quantile of the quantity of interest, as Sabater [42] describes.

One of the important components in building surrogate models is the sampling strategy used for evaluating the objective and constraint functions. Different Design of experiments (DOE) techniques aim to make data analysis more efficient by creating superior sampling methods. Among these, Latin hypercube sampling (LHS), introduced by McKay et al. [37], is arguably one of the most widely adopted approaches.

As a general guideline, when approximating an objective function with a Gaussian process, the initial number of design values should comprise roughly ten times as many samples as there are input dimensions [33].

The Surrogate Modelling for Aero-Data Toolbox (SMARTy), developed by DLR (German Aerospace Center), is employed both for generating the initial DOE and for constructing the kriging surrogate model [27, 7].

After the initial samples have been evaluated, a surrogate model is fitted. The objective function is approximated by kriging using Bayesian statistics [22, 27]. A comprehensive description of kriging construction can be found in Forrester [21]. In this work, universal kriging with a squared exponential Gaussian kernel is used. The hyperparameters are tuned by the maximum likelihood [56]. The resulting optimization problem is solved using differential evolution [47] to predict the global optimum.

A regularization constant, is added to better accommodate for noisy data. The expected improvement (EI) is then defined as the product of the potential improvement and its associated probability [29]. The EI criterion frequently proves to be the most effective strategy for locating a global minimum [42].

In high-dimensional, nonlinear problems, like aerodynamic analyses that involve shock waves, the convergence achieved by the preceding phase is not always assured. To address this, a trust region (TR) strategy is employed. It is a local exploitation technique that seeks the minimum within the vicinity of the current best sample [1].

For 2D optimization cases the Expected Hypervolume Improvement ($EHVI$) was derived, which is a generalization of the EI [18, 55]. The $EHVI$ is applied for the 2D design objective space, e.g. A_{min} over $C_{D\ min}$, necessary for the outer optimization loop, discussed in the following section 4.3.1.

4.3.1. Outer Loop - Flap Size Optimization

Figure 7 illustrates the general approach and methodology. The outer optimization layer (*Flap Size Optimizer*) provides the flap length and width, calculated from the inner and outer position for the top and bottom flaps, resulting in six optimization parameters $(l_s, w_l, w_r)_{Top,Bottom}$.

Within each iteration of the outer loop, a given set of values including the waverider geometry are transferred to the inner optimization loop (*Trim Optimizer*), which is exemplary illustrated in figure 8.

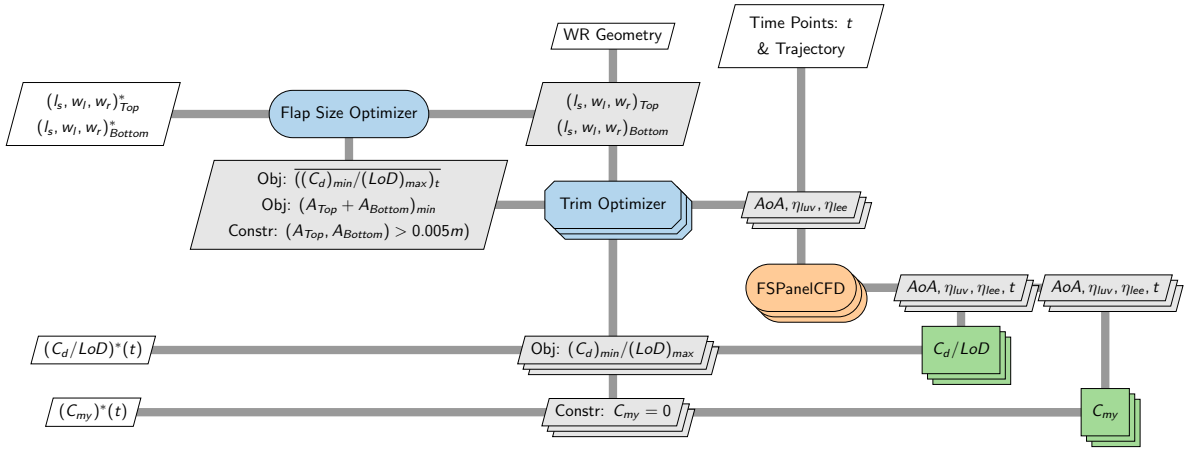

Fig 7. Multi target, multi objective, multi point optimization applied in SMARTy.

The flaps are cut from the initial geometry and a panel mesh is created automatically on each surface and given to the inner loop, called the *Trim Optimizer*, described in 4.3.2 in more detail.

The objective values are returned to the outer *Flap Size Optimizer* with the additional objective to minimize the size of each flap at the top and bottom $A_{Flaps,min} = (A_{Top} + A_{Bottom})_{min}$. A further constraint dictates to have a minimal flap size of $(A_{Top}, A_{Bottom}) > 0.005\,\text{m}$ for either side.

4.3.2. Inner Loop - Trim Optimization

The inner optimization loop uses the top and bottom flap deflection angles as its design variables and uses the given angle of attack, from the presented reference trajectory for the simulation results of the minimal possible drag coefficient (C_D), presented in section 5.1.

For the maximum lift over drag LoD optimization, presented in section 5.2, the inner loop additionally to the flap deflection angles it predicts the possible set of angle of attack to achieve maximum LoD. The return values are minimal C_D or maximum LoD respectively.

Both optimization runs have $C_{my} = 0$ as their constraint to only get pitch trimmed values within the optimization runs. If the given input values, regarding flap sizes, deflection angles and angle of attack can not satisfy the constraint, i.e. can not be trimmed within the given limits, the inner loops returns the failed state as a miss. This information gets evaluated as further information within SMARTy as well.

To limit the number of possible parameters in the design space, the optimization constraints of the angle of attack α are from $-5°$ to $20°$. The leeward as well as windward deflection angles can be varied from $0°$ to $20°$ each defined to deflect to the outside of the vehicle.

Figure 8(a) plots the DOE initiated by the LHS as grey points. Initially 50 iterations are performed, which results in the grey lines in figure 8(b). After the initial iterations, the surrogate model generates its expected improvement points, with a maximum of additional 20 points, calculating the green dots (fig. 8(a)), resulting in the green convergence history (fig. 8(b)). It can be seen, that only values near the optimal point of $C_{my} = 0$ at minimal C_D are evaluated and further improved with the TR method, with another additional 20 points at maximum, resulting in the best value plotted in blue, as depicted in figure 8(c).

This value gets returned to the outer optimizer as the best possible set of flap deflection angles for a trimmed geometry at a certain angle of attack with the given flap sizes. The inner trimming loops gets evaluated in parallel at every of the shown 23 trajectory points of figure 1. Each trimming loop needs about 1 min on a common workstation computer core. As it is distributed on every possible core, the

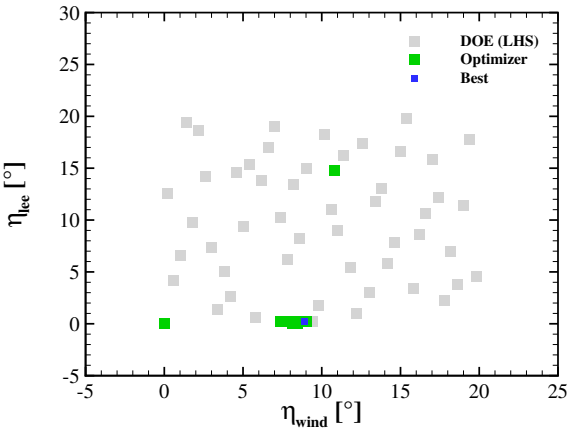

(a) DOE of inner optimization loop.

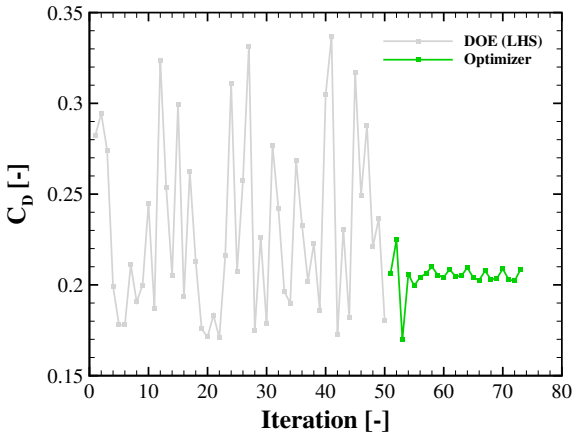

(b) Convergence history of objective value.

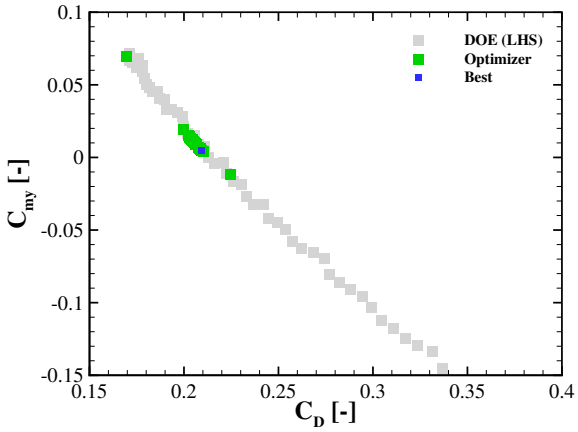

(c) Evaluated objective function and calculated Pareto front.

Fig 8. Inner optimization loop for pitch trimmed static analysis within SMARTy.

evaluation along the trajectory can easily be speed up in parallel, resulting in approximately 2 min for each outer loop iteration.

After evaluating each of the 23 trajectory points, and the given objective and constraint function values, the optimized flap sizes are analyzed and discussed in section 5. The complexity of the methodology can be described as a multi-target, multi-objective, multi-point optimization.

5. Flap Optimization Results

In the following chapter, two optimization targets are explored for the presented combination of reference geometry and trajectory. At first, a drag optimization in section 5.1, following the reference angle of attack along the trajectory, to get a flyable size of flaps at minimal drag. Later on, a lift over drag optimization get analysed, increasing the freely adjustable variables for the optimizer by incorporating the trim angle of attack in section 5.2.

5.1. C_D Optimization

Similar to the inner trim optimization, the initial evaluation points of the outer loops are selected by 50 LHS sample points, shown by grey dots in figure 9(a). Each of the points, represents the mean value of C_D of the 23 trajectory points with a constant stepping of $\Delta t = 20\,\mathrm{s}$, as illustrated in figure 1. That means, each of the dots calculates 23 trajectory points with individual 90 trim optimization calculations.

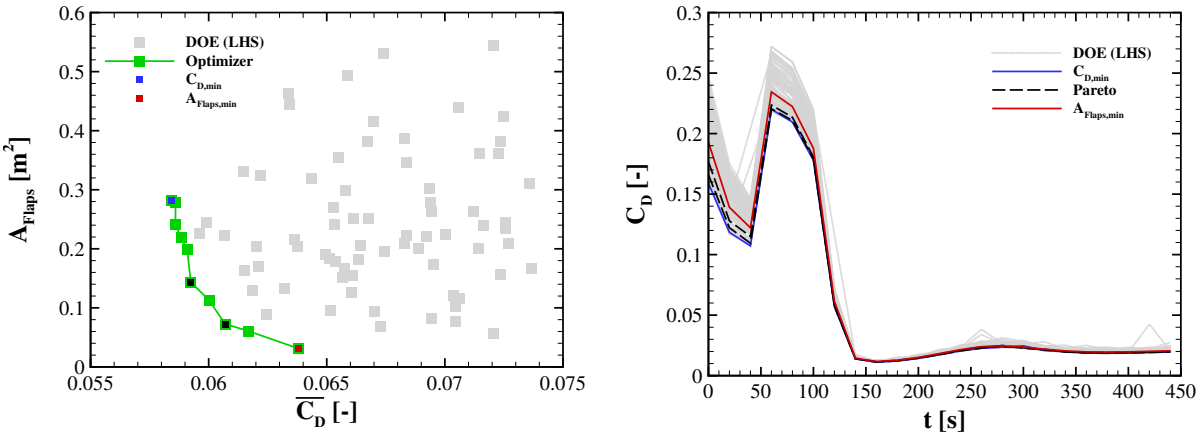

(a) DOE and optimization points.

(b) Evaluated variants of minimal C_D along the trajectory, resulting from the inner trim optimization.

Fig 9. DOE and optimization points including the evaluated objective function values for C_D optimization at 23 individual trajectory points.

After the initial DOE prediction additional 20 *EHVI* iterations, highlighted in green in figure 9(a), are performed to get the Pareto front between the best objective function values, minimal drag C_D and minimal flap area A_{Flaps}. Including every step, the total number of individual panel simulations add up to 124 200 iterations for the complete optimization process, which correlates to about 12 h of wall-clock time on a standard workstation when parallelized over all trajectory points.

As it is a two dimensional optimization problem, there can not be a single best value for the flap sizing. To look into possible flap combinations the minimal C_D, displayed in *blue*, and minimal flap sizes, displayed in *red*, are picked. To show some possible variations two further points on the Pareto front are marked in *black*.

Figure 9(b) presents every calculated set of combinations for each flight point at its specific time along the trajectory from 0 s to 440 s trimmed to minimize drag at the given reference angle of attack. As expected, the optimized minimal C_D flaps result in the smallest drag values, not only in average, but along the complete trajectory range.

The optimized configuration with the smallest flap size $A_{Flap,min}$ results in a bigger drag over time, which mainly corresponds in the much bigger necessary deflection angle to hold the given pitch trim angle of attack, as can be seen in figure 10. Figure 10(a) shows the lee side flap deflection angles on the top of the HLRV, which have a secondary effect for the trim angle, because the trim angle of attack is mainly positive during the reentry phase. This results in very small controlling forces and moments of the upper flaps, which makes it hard for the optimizer to access the necessity of the upper control surfaces. On the other side, the windward flaps on the bottom of the HLRV mainly affects the trim moments necessary for the wedge shaped main body. The optimized deflection angles shown in figure 10(b) show a lot of variation, especially between the selected four sets along the Pareto front.

The deflection limit of 20° for all control surfaces is represented in figure 10(b) as well. Only during the small frame between 40 s to 140 s the values succeed 10° for the bottom flaps of the vehicle to hold the trim angle for the case $A_{Flap,min}$. Optimized for minimum C_D. the deflection angles are under 10° along the whole trajectory, with values of under 5° during the gliding phase after $t = 250$ s. The two comparable sets of values on the Pareto front are between the discussed curves.

The resulting geometries and their resulting pitch trim deflection angle at time point $t = 80$ s are illustrated in figure 11. The optimization for $C_{D,min}$, shown in figure 11(a), moves the starting point of the flap downwards, compared to the initial geometry from figure 2. This effect can be seen in the other

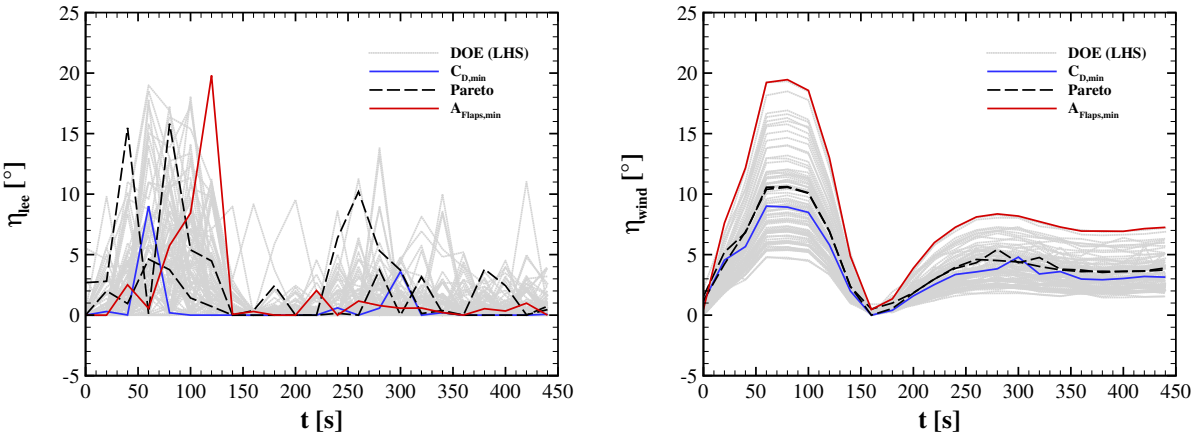

(a) η_{lee}. (b) η_{wind}.

Fig 10. Flap deflection angles of the top flap η_{lee} and bottom flap η_{wind} over time for C_D minimization.

variations as well. To reduce the drag as much as possible, the deflection angles are reduced, which needs the flap to be as wide as possible to get the same trimming moment, compared to the other variants. The top flap almost has no trimming effect, as discussed earlier. Looking along the Pareto front (figure 11(b) and 11(c)) the flap sizes gets smaller, till $A_{Flap,min} = 0.025\,\mathrm{m}^2$ is reached, shown in figure 11(d). As the flap size is much smaller compared to the $C_{D,min}$ case, the deflection angle are almost twice the amount, to achieve a trimmed state, which results in higher drag, as can be seen in figure 9(a).

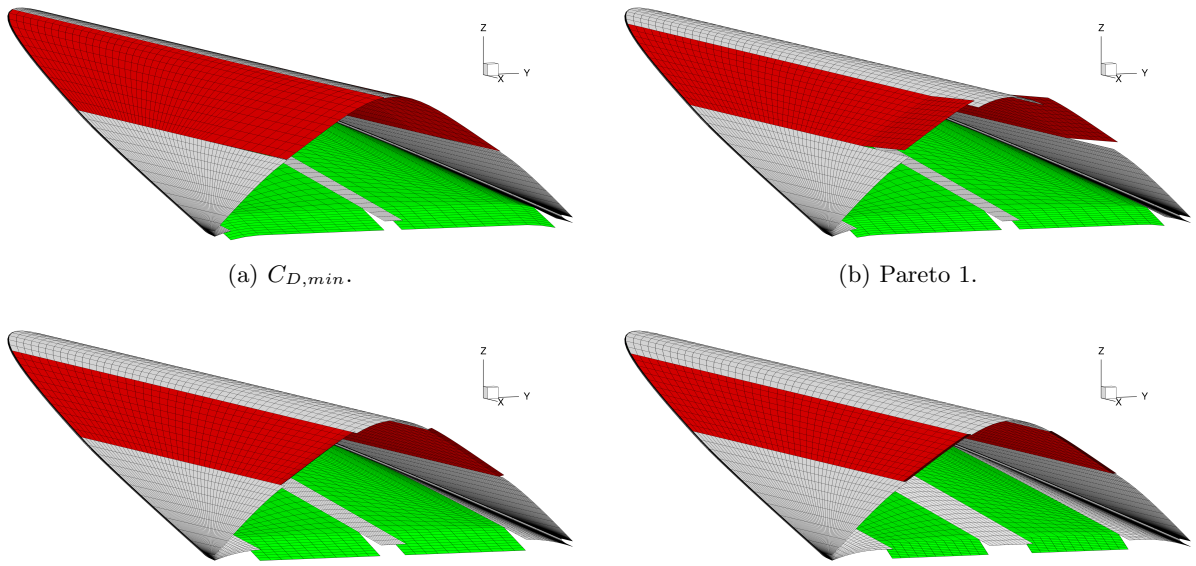

(a) $C_{D,min}$. (b) Pareto 1.

(c) Pareto 2. (d) A_{min}.

Fig 11. Best variants at $t = 80\,\mathrm{s}$ for C_D.

5.2. *LoD* Optimization

Building on the former optimization process, the angle of attack is taken into account to get an optimized pitch trimmed state, more independent from the initial reference trajectory, while optimizing for LoD_{max}. Again, the initial DOE (*grey* dots) is represented in 12(a), followed by the optimization iterations in *green*.

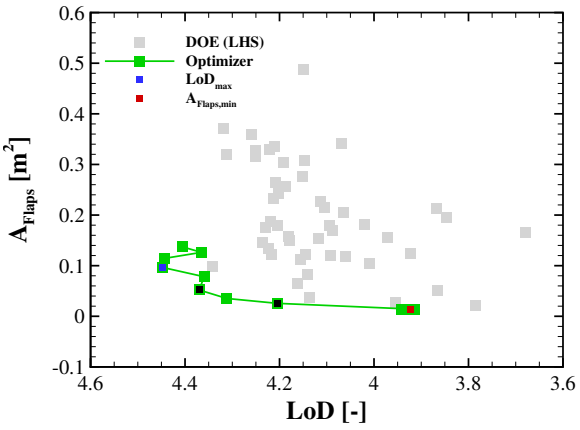

(a) DOE and optimization points.

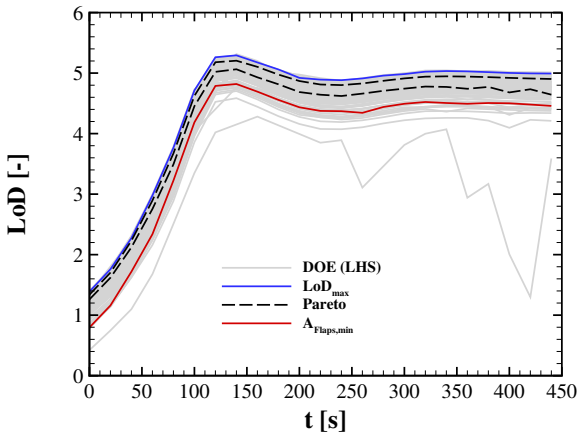

(b) Evaluated variants of LoD_{max} along the trajectory, resulting from the inner trim optimization.

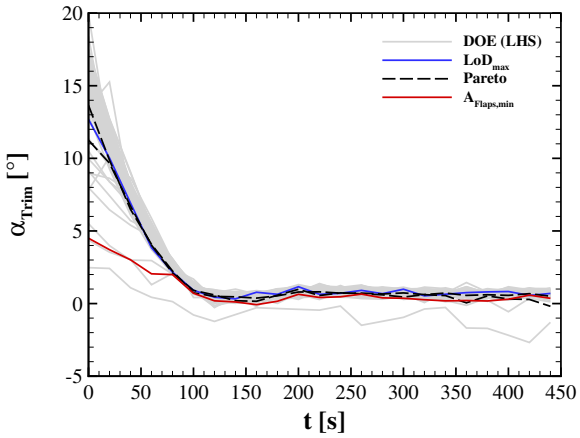

(c) Trimmed angle of attack along the trajectory, resulting from the inner trim optimization.

Fig 12. DOE and optimization points including the evaluated objective function values for LoD_{max} optimization and their corresponding trimmed angle of attack at 23 individual trajectory points.

The two dimensional objective optimization for minimal flap area over LoD_{max} gives a Pareto front of possible optimization sets, which will be condensed to the point of $A_{Flap,min}$ (in *red*) and LoD_{max} (in *blue*). It can be seen, that the optimization iterations vary much more, with significant differences from the Pareto front, compared to the iteration from the former $C_{D,min}$ optimization in section 5.1.

The optimized LoD curve for the flap set of LoD_{max} is shown in figure 12(b) with values of up to 5.4 during the reentry and about 5 during the gliding phase. The flap set for $A_{Flap,min}$ reduces LoD to about 4.8 and 4.4 respectively. The two representative Pareto points are between. Especially at the beginning of the trajectory, the bigger LoD for the LoD_{max} variation comes from a much higher trim angle, shown in figure 12(c). During the gliding phase the expected trim angle is between 0° to 2° for most of the configurations.

In line with former section 5.1, the flaps of the upper leeside of the HLRV do not contribute much to the resulting trim moment, because they are not in the flow due to the solely positive trim angles along the trajectory, which results in the deflection plots of figure 13(a).

The flap deflection angle of the bottom side do the main trimming moment, varying much between the

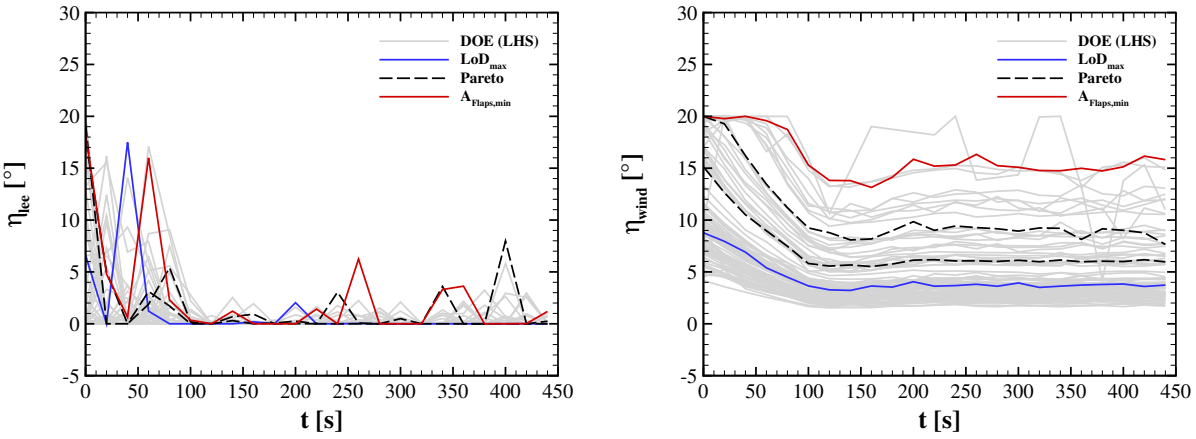

(a) n_{lee}. (b) n_{wind}.

Fig 13. Flap deflection angles over time for LoD.

evaluated iterations of flap sizing, as shown in figure 13(b). For the LoD_{max} case, the deflection angles are starting at 9° converging towards 4° at the end of the trajectory, while the values for the $A_{Flap,min}$ case start at the maximum of 20° and reaching around 15° in the gliding phase. As expected, the later can be explained by the much smaller flaps, which are illustrated in figure 14(b). On a first glance, the flaps seems to be unrealistic small, which might indicate an edge case of the combination of optimization technique and validity of the low-fidelity solver. To get a better insight, a multi-fidelity analysis should be performed at this stage to validate the results, as described by Barz [5]. This is not part of the current paper, but will be performed in succeeding work in the near future.

Furthermore, the flap sizing of bottom flaps of the LoD_{max} (figure 14(a)) and $C_{D,min}$ (figure 11(a)) case overlap with each other. The Area of the flap of the $C_{D,min}$ optimization results in $A_{Bottom} = 0.084\,\mathrm{m}^2$ with a width of $w_{Bottom} = 0.476\,\mathrm{m}$, almost exactly matching the values for the LoD_{max} optimization of $A_{Bottom} = 0.085\,\mathrm{m}^2$ with a width of $w_{Bottom} = 0.476\,\mathrm{m}$. This can be explained by the major influence of drag in LoD for this kind of geometries, because they usually generate significant lift at very small angles of attack due to their wedge like form.

Both optimization procedures predict very small upper flap areas. As already discussed, in both cases they are in the leeward side of the main body, which minimizes their efficiency. Furthermore, the lack of transient effects in the presented work needs to be assessed. Every point on the trajectory was analysed as steady condition. The necessary lift force to pull the dipping maneuver to stay on the flight path was not evaluated. This will mainly be achieved by the upper flaps, which will then increase in size during the optimization loop. This will be implemented and analysed in further work.

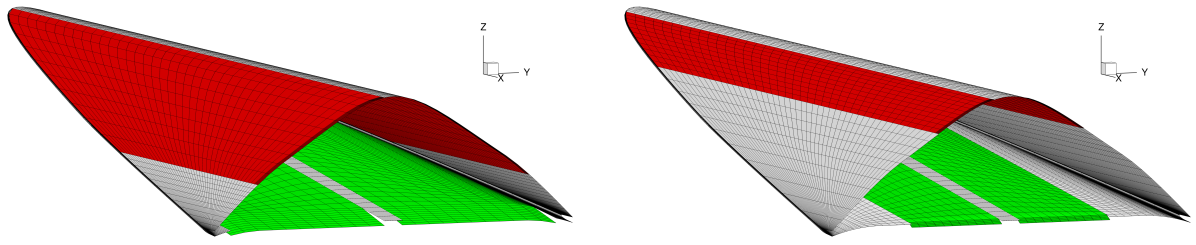

(a) LoD_{max}. (b) A_{min}.

Fig 14. Best variants at $t = 80\,\mathrm{s}$ for LoD.

6. Conclusion

This paper has demonstrated that a low-fidelity workflow can be used to assess and optimize the aerodynamic flight-stability performance of a high-lift reentry vehicle (HLRV) along a complete hypersonic trajectory. The paper presented the validation of the used low-fidelity panel methods. By combining the Modified-Newton (*MN*) model for the blunt leading-edge region with the Shock-Expansion (*SE*) model for the remaining surfaces (the *Combined* method), the *FSPanelCFD* code implemented in the CoNF^{2}aS^2 process chain, reproduces the high-fidelity DLR TAU results with errors below 11 % for the axial force, 7 % for the normal force and 3 % for the pitching moment when friction is included. This level of agreement is sufficient to capture the overall trend of the aerodynamic loads and to serve as a surrogate for rapid design-space exploration. Furthermore a simple static pitch-stability has been performed. Using the validated low-fidelity model, the static stability envelope of the reference waverider was mapped for the entire trajectory. A centre-of-gravity location at around 60 % of the vehicle length guarantees static stability with trimmed flap actuation. Free-flight simulations confirm that the baseline vehicle can be trimmed with flap deflections less than 4° for trim angles between 2° to −3° throughout the flight, depending on the center of gravity.

Afterwards a surrogate-based optimisation of flap geometry has been introduced and presented. The DLR-SMARTy toolbox was employed to build kriging surrogates for the aerodynamic response at 23 equally-spaced points along the trajectory. Two multi-objective optimization problems were solved:

1. Drag minimization ($C_{D,min}$): The Pareto front between drag and total flap area shows that a modest bottom flap size of 0.085 m^2 per side results in the minimal drag while keeping flap deflections below 5° during the gliding phase. The smallest feasible flap area can still be used, but requires deflection angles close to the 20° limit and consequently incurs a higher drag penalty.

2. Lift-over-drag maximization (LoD_{max}): Maximizing *LoD* yields a similar flap size as the drag minimisation case because the waverider's wedge-shaped body already provides high lift at low angles of attack. The optimal configuration attains a peak *LoD* of 5.4 during reentry and around 5.0 in the glide phase, with flap deflections remaining below 10° for the larger flaps and approaching the 20° limit for the smallest flaps.

The multi-objective optimization capabilities give designers explicit trade-offs between aerodynamic performance (C_D or *LoD*) and mechanical constraints (flap area, deflection limits). This information is essential for integrated vehicle-system optimisation, where mass, structural stiffness and thermal-protection requirements must be balanced against aerodynamic efficiency. The demonstrated workflow is readily extensible to additional design variables (e.g., leading-edge radius, body-flare sweep, material properties) and to other flight-mechanics constraints, like dynamic stability or control-rate limits.

The hierarchical optimization strategy (outer flap-size loop, inner trim-angle loop) represents a speed-up of several orders of magnitude compared with a full high-fidelity CFD-FSI simulation, thereby enabling rapid design iterations by providing a powerful and computationally efficient tool for the early-stage design of high-lift hypersonic reentry vehicles. By bridging the gap between rapid concept evaluation and high-fidelity verification within CoNF^{2}aS^2, it paves the way for more systematic, integrated optimisation of future hypersonic spacecrafts.

The low-fidelity panel method neglects viscous effects between the flaps and the main body, real-gas effects and three-dimensional shock-boundary-layer interactions. Although the overall trends are captured, local pressure peaks and heating rates may be under-predicted, especially in the highly non-equilibrium regime of mach number greater than 10, which will be taken into account in further studies by applying a multi fidelity approach. Furthermore, the required flap-deflection rates and associated actuator dynamics remain to be verified to access the pull up performance of the reference geometry.

Overall, the presented optimization procedure opens up the wide range of optimization strategies integrated within DLR-SMARTy, enhancing spacecraft design on a much broader operational range. Combined with the efficient aerothermal load prediction presented in [24], this framework will further improve thermal protection system design, crucial for long-duration hypersonic missions.

7. Funding
The authors gratefully acknowledges the CFD development team at the German Aerospace Center (DLR), as well as the scientific support and HPC resources provided by DLR. The HPC system CARA is partially funded by the "Saxon State Ministry of Economic Affairs, Labour and Transport" and the "Federal Ministry of Economics and Climate Protection". The HPC system CARO is partially funded by "Ministry of Science and Culture of Lower Saxony" and "Federal Ministry for Economic Affairs and Climate Action".

8. Conflict of interest
No conflicts of interest were identified.

References
[1] N. M. Alexandrov, J. E. Dennis, R. M. Lewis, and V. Torczon. A trust-region framework for managing the use of approximation models in optimization. *Structural Optimization*, 15(1):16–23, February 1998.

[2] John D. Anderson. *Hypersonic and High-Temperature Gas Dynamics*. American Institute of Aeronautics and Astronautics, Washington D.C., USA, 3rd edition edition, April 2019.

[3] Tarik Barth. Aero- and Thermodynamic Analysis to SHEFEX I. *Engineering Applications of Computational Fluid Mechanics*, 1(1), 2007.

[4] Fynn Barz. Comparison of Different Fidelity Approaches for the Coupled Aerothermodynamic Heating of Blunt Leading Edge High Lift Reentry Vehicles. In *24th STAB Symposium*, Regensburg, 2024.

[5] Fynn Barz. Multi-Fidelity Shape Optimization of a High Lift Reentry Vehicle for a Suborbital Reentry Mission. In *HiSST: 4th International Conference on High-Speed Vehicle Science Technology*, Tours, France, September 2025.

[6] Fynn Barz and Marius Franze. Comparison of Different Fidelity Approaches for the Coupled Aerothermodynamic Heating of Hypersonic Reentry Vehicle. In *HiSST: 3rd International Conference on High-Speed Vehicle Science Technology*, Busan, Korea, April 2024.

[7] Philipp Bekemeyer, Anna Bertram, Derrick Armando Hines Chaves, Mateus Dias Ribeiro, Andrea Garbo, Christian Sabater Campomanes, Mario Stradtner, Simon Wassing, Markus Widhalm, Stefan Görtz, Florian Jäckel, Robert Hoppe, and Nils Hoffmann. Data-Driven Aerodynamic Modeling Using the DLR SMARTy Toolbox. In *AIAA Aviation*, Chicago, USA, 2022.

[8] Shanti Bhushan, Greg W. Burgreen, Anup Zope, Parker Bailey, and Ian D. Dettwiller. Hypersonic Trajectory Optimization for Minimum Heating Using Machine Learned Physics Surrogates. In *AIAA AVIATION FORUM AND ASCEND 2024*, Las Vegas, Nevada, July 2024. American Institute of Aeronautics and Astronautics.

[9] K. G. Bowcutt, John D. Anderson, and D. Capriotti. Viscous optimized hypersonic waveriders. In *25th AIAA Aerospace Sciences Meeting*, Reno, NV, USA, 1987-01-12/1987-01-15. American Institute of Aeronautics and Astronautics.

[10] Jonathan Cangelosi, Matthias Heinkenschloss, Jacob T. Needels, and Juan J. Alonso. Simultaneous Design and Trajectory Optimization for Boosted Hypersonic Glide Vehicles. In *AIAA SCITECH 2024 Forum*, Orlando, FL, January 2024. American Institute of Aeronautics and Astronautics.

[11] José Carvalho and Erwin Mooij. Integrated Shape and Trajectory Optimisation of Hypersonic Waveriders. In *AIAA SCITECH 2024 Forum*, Orlando, FL, January 2024. American Institute of Aeronautics and Astronautics.

[12] David S. Ching, Patrick J. Blonigan, and Jonathan C. Murray. Reduced Order Models of Hypersonic Aerodynamics for Aerothermal Heating Analysis. In *AIAA SCITECH 2024 Forum*, Orlando, FL, January 2024. American Institute of Aeronautics and Astronautics.

[13] David S. Ching, Patrick J. Blonigan, Francesco Rizzi, and Jeffrey A. Fike. Reduced Order Modeling of Hypersonic Aerodynamics with Grid Tailoring. In *AIAA SCITECH 2022 Forum*, San Diego, CA & Virtual, January 2022. American Institute of Aeronautics and Astronautics.

[14] Justin M. Cooper and Alexandre Martin. Novel Engineering Methodology for Decoupled Aerothermal Analysis of Hypersonic Atmospheric Entry Flows. *Journal of Spacecraft and Rockets*, 60(2):437–453, March 2023.

[15] Kyle A. Damm, Rowan Gollan, and Anand Veeraragavan. Trajectory-Based Conjugate Heat Transfer Simulation of the BoLT-II Flight Experiment. In *AIAA SCITECH 2023 Forum*, National Harbor, MD & Online, January 2023. American Institute of Aeronautics and Astronautics.

[16] E. R. G. Eckert. Engineering Relations for Heat Transfer and Friction in High-Velocity Laminar and Turbulent Boundary-Layer Flow Over Surfaces With Constant Pressure and Temperature Available. *Transactions of the American Society of Mechanical Engineers*, 78(6):1273–1283, August 1956.

[17] Thino Eggers. *Aerodynamischer Entwurf von Wellenreiter - Konfigurationen für Hyperschallflugzeuge*. PhD thesis, Technische Universität Braunschweig, Deutschland, 1999.

[18] Michael T. M. Emmerich, Andre H. Deutz, and Jan Willem Klinkenberg. Hypervolume-based expected improvement: Monotonicity properties and exact computation. In *2011 IEEE Congress of Evolutionary Computation (CEC)*, pages 2147–2154, New Orleans, LA, USA, June 2011. IEEE.

[19] Nathan Falkiewicz, Carlos Cesnik, Andrew Crowell, and Jack McNamara. Reduced-Order Aerothermoelastic Framework for Hypersonic Vehicle Control Simulation. In *AIAA Atmospheric Flight Mechanics Conference*, Toronto, Ontario, Canada, August 2010. American Institute of Aeronautics and Astronautics.

[20] J. A. Fay and F. R. Riddell. Theory of Stagnation Point Heat Transfer in Dissociated Air. *Journal of the Aerospace Sciences*, 25(2):73–85, February 1958.

[21] Alexander I. J. Forrester, András Sóbester, and Andy J. Keane. *Engineering Design via Surrogate Modelling: A Practical Guide*. Wiley, 1 edition, July 2008.

[22] Alexander I.J. Forrester and Andy J. Keane. Recent advances in surrogate-based optimization. *Progress in Aerospace Sciences*, 45(1-3):50–79, January 2009.

[23] Marius Franze. *Flugbahnanalyse Eines Raumfahrzeuges Mittels Multidisziplinärer Kopplung*. PhD thesis, Deutsches Zentrum für Luft- und Raumfahrt e. V. (DLR), 2024.

[24] Marius Franze and Fynn Barz. Comparison of models for aerothermal load prediction using coupled trajectory simulations of a high lift reentry vehicle. *CEAS Space Journal*, January 2025.

[25] Maxim Freydin and Earl H. Dowell. Fully Coupled Nonlinear Aerothermoelastic Computational Model of a Plate in Hypersonic Flow. *AIAA Journal*, 59(7):2725–2736, July 2021.

[26] Jonah R. Gottlieb, John M. Mines, Daniel C. Garmendia, Jerold W. Emhoff, and Daniel E. Clemens. Coupled Vehicle and Trajectory Design Optimization for Boost-Glide Hypersonic Systems. In *AIAA SCITECH 2024 Forum*, Orlando, FL, January 2024. American Institute of Aeronautics and Astronautics.

[27] Zhong-Hua Han, Stefan Görtz, and Ralf Zimmermann. Improving variable-fidelity surrogate modeling via gradient-enhanced kriging and a generalized hybrid bridge function. *Aerospace Science and Technology*, 25(1):177–189, March 2013.

[28] Jennifer Horing, Kurt K. Maute, and Iain D. Boyd. Coupling Strategies for Analyzing Fluid-Thermal-Structural Interactions of a Hypersonic Inlet. In *AIAA SCITECH 2024 Forum*, Orlando, FL, January 2024. American Institute of Aeronautics and Astronautics.

[29] Donald R. Jones, Matthias Schonlau, and William J. Welch. Efficient Global Optimization of Expensive Black-Box Functions. *Journal of Global Optimization*, 13(4):455–492, December 1998.

[30] Michael Jones and Carlos E. Cesnik. Performance Analysis of Kriging and Neural Network Modelling of Hypersonic Vehicle Properties. In *AIAA SCITECH 2023 Forum*, National Harbor, MD & Online, January 2023. American Institute of Aeronautics and Astronautics.

[31] L. G. Kaufman, II. Pressure estimation techniques for hypersonic flows over blunt bodies. *Journal of Astronautical Sciences*, 1963.

[32] Stefan Langer, Axel Schwöppe, and Norbert Kroll. The DLR Flow Solver TAU - Status and Recent Algorithmic Developments. In *52nd Aerospace Sciences Meeting*, National Harbor, Maryland, January 2014. American Institute of Aeronautics and Astronautics.

[33] Jason L. Loeppky, Jerome Sacks, and William J. Welch. Choosing the Sample Size of a Computer Experiment: A Practical Guide. *Technometrics*, 51(4):366–376, November 2009.

[34] A. Mack and Volker Hannemann. Validation of the Unstructured DLR-TAU-Code for Hypersonic Flows. In *32nd AIAA Fluid Dynamics Conference and Exhibit, AIAA Paper 2002-3111*, pages 1–9, St. Lousi, Missouri, 2002.

[35] Andreas Mack and Roger Schaefer. Fluid Structure Interaction on a Generic Body-Flap Model in Hypersonic Flow. *Journal of Spacecraft and Rockets*, 42(5):769–779, September 2005.

[36] Alexandre Martin and Iain D. Boyd. Strongly Coupled Computation of Material Response and Nonequilibrium Flow for Hypersonic Ablation. *Journal of Spacecraft and Rockets*, 52(1):89–104, January 2015.

[37] M. D. McKay, R. J. Beckman, and W. J. Conover. Comparison of Three Methods for Selecting Values of Input Variables in the Analysis of Output from a Computer Code. *Technometrics*, 21(2):239–245, May 1979.

[38] Michael Meinel and Gunnar ´Olafur Einarsson. The FlowSimulator framework for massively parallel CFD applications. In *State of the Art in Scientific and Parallel Computing*, University of Iceland, Reykjavi, 2010-06-06/2010-06-09.

[39] NOAA, NASA, and U.S. Air Force. U.S. Standard Atmopshere 1976. Report NASA-TM-X74335, Washington D.C., USA, 1976.

[40] Farid K. Rafla. Aerodynamic Heating Coupled with Structural Temperature Response Analysis for Hypersonic Flight Vehicles. In *AIAA Aviation 2019 Forum*, Dallas, Texas, June 2019. American Institute of Aeronautics and Astronautics.

[41] Lars Reimer, Ralf Heinrich, Sven Geisbauer, Tobias Leicht, Stefan Görtz, Markus Raimund Ritter, and Andreas Krumbein. Virtual Aircraft Technology Integration Platform: Ingredients for Multidisciplinary Simulation and Virtual Flight Testing. In *AIAA Scitech 2021 Forum*, Virtual Event, January 2021.

[42] Christian Sabater, Philipp Bekemeyer, and Stefan Görtz. Efficient Bilevel Surrogate Approach for Optimization Under Uncertainty of Shock Control Bumps. *AIAA Journal*, 58(12):5228–5242, December 2020.

[43] Aravinth Sadagopan, Daning Huang, Adam Jirasek, Jürgen Seidel, Anshuman Pandey, and Katya M. Casper. Hypersonic Fluid–Thermal–Structural Interaction of Cone–Slice–Ramp: Computations with Experimental Validation. *AIAA Journal*, 61(11):4752–4771, November 2023.

[44] Andreas Schütte. *Wirbelumströmungen an gepfeilten Flügeln mit runden Vorderkanten*. DLR Forschungsbericht 2015-40, Dissertation, Technische Universität Braunschweig, Deutschland, 2015.

[45] Dieter Schwamborn, Thomas Gerhold, and Ralf Heinrich. The DLR TAU-Code: Recent Applications in Research and Industry. *European Conference on Computational Fluid Dynamics, ECCOMAS CFD*, pages 1–25, 2006.

[46] Philippe R. Spalart and Steven R. Allmaras. A One-Equatlon Turbulence Model for Aerodynamic Flows. In *30th Aerospace Sciences Meeting & Exhibit*, Reno, Nevada, USA, 1992.

[47] Rainer Storn and Kenneth Price. Differential Evolution – A Simple and Efficient Heuristic for global Optimization over Continuous Spaces. *Journal of Global Optimization*, 11(4):341–359, December 1997.

[48] Wei-Yi Su, Hang An, and Mou-Yuan Wang. Fluid–Thermal–Structure Interaction of Hypersonic Inlets Under Different Aspect Ratios. *AIAA Journal*, 61(9):3722–3734, September 2023.

[49] Kyriakos C. Tapinou, Ingo Jahn, and Peter Jacobs. Hypersonic Fluid–structure interactions with elastic deformation and viscous effects (part of AePW3). In *AIAA SCITECH 2024 Forum*, Orlando, Florida, USA, January 2024. American Institute of Aeronautics and Astronautics.

[50] Chinmay S. Upadhye and Daniel J. Bodony. Investigating Fluid-Thermal-Structure Interactions of Hypersonic Control Fins. In *AIAA SCITECH 2024 Forum*, AIAA SciTech Forum, Orlando, FL, January 2024. American Institute of Aeronautics and Astronautics.

[51] Yasuh Wada and Meng-Sing Liou. An Accurate and Robust Flux Splitting Scheme for Shock and Contact Discontinuities. 18(3):633–657, 1997.

[52] Ruixing Wang, Zhaowei Wang, Hongwei Zheng, and Hongwei Song. Comparison of Strategies for Coupled Flow-Thermal Analysis of Thermal Protection System at Hypersonic Flight Condition. *International Journal of Aeronautical and Space Sciences*, 21(2):347–362, June 2020.

[53] Viola Wartemann, Marius Franze, Sebastian Jack, Fynn Barz, and Bodo Reimann. Current Status and Applications of CoNF2aS2 - Coupled Numerical Fluid-Flight Mechanics and Structural Simulation. In *4th HiSST - International Conference on High-Speed Vehicle Science Technology*, Tours, France, September 2025.

[54] Bradley M. Wheaton and Aaron T. Dufrene. Preflight and Postflight Thermal/Structural Analysis of BOLT II: The Holden Mission. *Journal of Spacecraft and Rockets*, 61(5):1204–1218, September 2024.

[55] Kaifeng Yang, Michael Emmerich, André Deutz, and Thomas Bäck. Efficient computation of expected hypervolume improvement using box decomposition algorithms. *Journal of Global Optimization*, 75(1):3–34, September 2019.

[56] Ralf Zimmermann. Asymptotic Behavior of the Likelihood Function of Covariance Matrices of Spatial Gaussian Processes. *Journal of Applied Mathematics*, 2010(1):494070, January 2010.